



Probing molecular environment through photoemission delays

Shubhadeep Biswas^{1,2}, Benjamin Förg^{1,2}, Lisa Ortmann^{3,4}, Johannes Schötz^{1,2}, Wolfgang Schweinberger^{1,5}, Tomáš Zimmermann^{3,6}, Liangwen Pi³, Denitsa Baykusheva⁷, Hafiz A. Masood⁵, Ioannis Liontos⁵, Amgad M. Kamal⁵, Nora G. Kling¹, Abdullah F. Alharbi⁸, Meshaal Alharbi⁵, Abdallah M. Azzeer⁵, Gregor Hartmann^{9,10}, Hans J. Wörner⁷, Alexandra S. Landsman^{3,4,11}✉ and Matthias F. Kling^{1,2}✉

Attosecond chronoscopy has revealed small but measurable delays in photoionization, characterized by the ejection of an electron on absorption of a single photon. Ionization-delay measurements in atomic targets provide a wealth of information about the timing of the photoelectric effect, resonances, electron correlations and transport. However, extending this approach to molecules presents challenges, such as identifying the correct ionization channels and the effect of the anisotropic molecular landscape on the measured delays. Here, we measure ionization delays from ethyl iodide around a giant dipole resonance. By using the theoretical value for the iodine atom as a reference, we disentangle the contribution from the functional ethyl group, which is responsible for the characteristic chemical reactivity of a molecule. We find a substantial additional delay caused by the presence of a functional group, which encodes the effect of the molecular potential on the departing electron. Such information is inaccessible to the conventional approach of measuring photoionization cross-sections. The results establish ionization-delay measurements as a valuable tool in investigating the electronic properties of molecules.

The advent of high-intensity ultrashort lasers, awarded with the Nobel prize in physics in 2018, enabled the reconstruction of fundamental processes inside atoms and molecules on the attosecond (as) timescale¹. One such process is Einstein's photoelectric effect, characterized by electron emission on the absorption of a single photon. It proved the discrete nature of light and was instrumental to the subsequent development of quantum mechanics. The target-specific delay of this photoemission process is given by the Eisenbud–Wigner–Smith (EWS) delay, which relates photoemission to a half-scattering event, and can be calculated from the energy derivative of the phase of the ionized electron wavepacket². This time delay provides important information on the electronic structure of matter, which includes electron correlations and the details of the atomic or molecular potential in which electrons move. These can help us develop and validate theoretical models that describe electronic excitations in molecules.

Attosecond time delays in photoemission have been studied extensively in the past decade using streaking^{3–6} or RABBITT^{7–12} experiments, which combine a weak isolated attosecond pulse (IAP) or pulse train, respectively, to perform single-photon ionization, with a probing infrared laser pulse. Such experiments^{3–11} and the wealth of theoretical studies they inspired^{13,14} were mainly confined to atomic targets. Recently, photoionization delays were measured in simple molecules^{7,11,15}. However, the physical interpretation of such experiments is extremely challenging for the following reasons.

First, it is extremely difficult to isolate a specific ionization channel in a molecule due to spectral congestion that results from closely spaced energy levels^{9,10,14}. Combined with the relatively broad bandwidth of an IAP, this often makes it impossible to assign the correct initial electronic states based on the final electron energies, even for simplest diatomic molecules¹¹. Second, the ionization process can be viewed as comprising two highly complex steps: the initial ionization of the electron, followed by a subsequent propagation in the molecular potential. As the electronic states involved in the ionization process are unique to that particular molecule, there is normally no reference to disentangle these two steps and separate the contribution of the molecular potential in which the ionized electron wavepacket moves.

Here we overcome these challenges by measuring attosecond ionization delays in a polyatomic molecule, ethyl iodide, around a giant dipole resonance. Unlike other resonances, being an inner shell characteristic, the giant dipole resonance is known to remain largely unaffected when an atom becomes part of a larger molecule: “If a ‘giant resonance’ is present in an atom, then we expect to find it, with perhaps slight variations of the profile shape, in molecules containing this atom, or indeed in the condensed phase. This persistence of the resonance is unique amongst excited atomic states, and contrasts sharply with Rydberg behaviour. It provides experimental confirmation that the effect originates deep inside the atom ...” (Connerade et al.¹⁶). This is illustrated for the *4d* resonance (see also Fig. 1b) in Fig. 1c, in which photoionization cross-sections

¹Physics Department, Ludwig-Maximilians-Universität Munich, Garching, Germany. ²Max Planck Institute of Quantum Optics, Garching, Germany.

³Max Planck Institute for the Physics of Complex Systems, Dresden, Germany. ⁴Department of Physics, The Ohio State University, Columbus, OH, USA.

⁵Attosecond Science Laboratory, Physics and Astronomy Department, King Saud University, Riyadh, Saudi Arabia. ⁶Department of Mathematics, ETH Zurich, Zurich, Switzerland. ⁷Laboratory of Physical Chemistry, ETH Zurich, Zurich, Switzerland. ⁸King Abdulaziz City for Science and Technology (KACST), Riyadh, Saudi Arabia. ⁹Helmholtz-Zentrum Berlin (HZB), Berlin, Germany. ¹⁰Institut für Physik, University of Kassel, Kassel, Germany. ¹¹Max Planck POSTECH/KOREA Research Initiative, Pohang, South Korea. ✉e-mail: landsman.7@osu.edu; matthias.kling@lmu.de

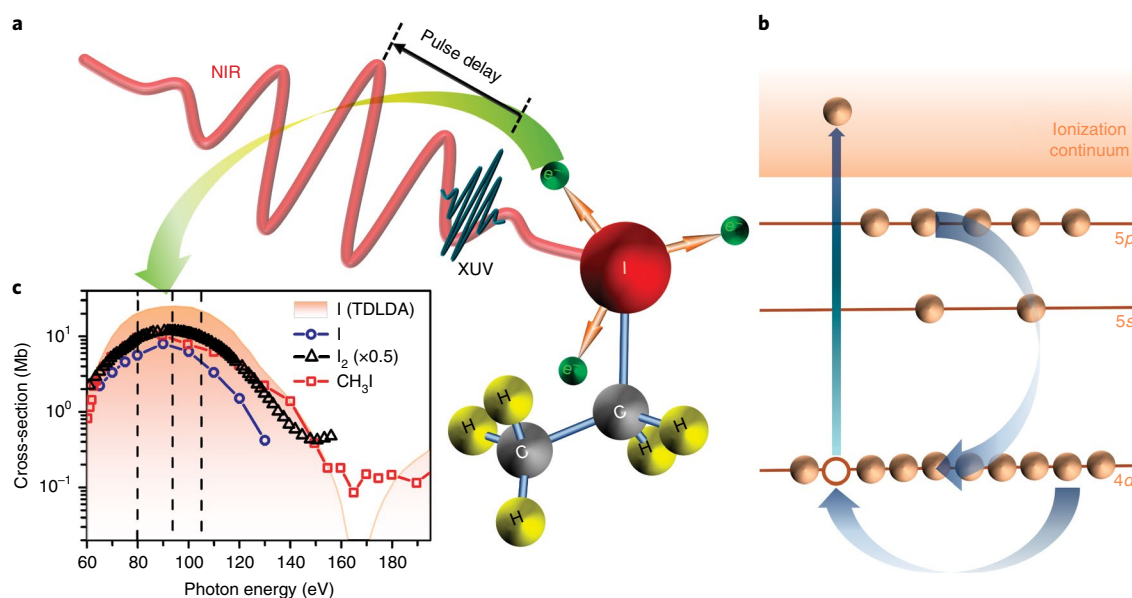


Fig. 1 | Photoemission delays around the giant 4d resonance in ethyl iodide. **a**, Few-cycle NIR and isolated XUV attosecond pulses with a variable delay are focused onto the target jet, which contains neon atoms and ethyl iodide molecules. Photoelectrons, emitted in a linear photoionization process from XUV photons, are propagated in the respective atomic and molecular orbitals in the presence of the NIR laser field. The delay-dependent final streaked photoelectron energies are analysed by a TOF detector, which yields the photoelectron streaking spectrogram. For ethyl iodide, the ionized 4d electrons sample the molecular environment during their propagation. **b**, The energy-level diagram depicts the scheme of the photoionization process, in which an electron from the 4d subshell of the iodine atom within ethyl iodide is emitted into the continuum. Intra- and intershell couplings of the photoelectrons, which result in a giant dipole resonance, are illustrated by the curved arrows. **c**, Photoionization cross-sections for atomic iodine calculated with time-dependent local density approximation (TDLDA) theory³¹ (orange shaded region) together with experimentally obtained photoionization cross-sections for different iodine-containing compounds, which include atomic²³ (blue circles) and molecular³⁴ iodine (black triangles) and methyl iodide³⁵ (red squares). The photoionization delays were analysed at different XUV photon energies, indicated by the vertical dashed lines at 80, 93 and 105 eV.

(the absolute values are subject to discussion in the literature¹⁷) for atomic and molecular iodine and an iodine-containing molecule are shown. In addition, the lifetime of a giant resonance is several orders of magnitude shorter than that of typical autoionizing states¹⁶. Consequently, any notable measured delays are largely incurred during the propagation step, and thereby provide information on the molecular potential landscape experienced by the escaping electron wavepacket. Hence, in the case of a giant dipole resonance in the iodine-containing molecule, the iodine atom provides a natural reference, which allows us to both identify the initial electron localization (deep inside the iodine atom) and subsequent ionization pathway, and disentangle the two steps of the ionization process. The first step refers to a dipole $4d \rightarrow 4f$ transition, with the corresponding giant resonance being very similar in both iodine and ethyl iodide. The second step refers to propagation of the freed electron in the atomic and molecular potential, respectively. Being able to disentangle the two steps of the ionization process therefore presents a unique opportunity to measure the effect of the molecular potential, in this case introduced by the ethyl group, on the propagation of an ionized electron wavepacket, initially localized around an iodine atom. We found that the addition of an ethyl group introduces an additional delay of up to around 38.0 ± 21.4 as, which indicates a substantial modification of the potential landscape observed by the escaping electron. Noteworthy, this occurs even though the ethyl group does not directly participate in the ionization process, with the hole being initially confined to the inner shells of the iodine atom, and without molecular orientation. Our study disentangles the effect of a functional group on ionization delays in a molecule, with possible implications for the timing of the electron transfer in chemical reactions. We note that the comparison of ionization cross-sections between atomic and molecular species contains information on the molecular environment during the initial

excitation step, whereas time-delay measurements, introduced here, provide information on the molecular environment as experienced by the liberated escaping electron during the propagation.

Results and discussion

The experimental approach, which employs attosecond streaking spectroscopy¹, is illustrated in Fig. 1a and described in detail in Methods. In brief, IAPs in the extreme ultraviolet (XUV) regime at 80 and 93 eV with a bandwidth of 6.5 eV were generated from phase-stabilized few-cycle near-infrared (NIR) laser pulses of less than 5 fs duration at a 750 nm central wavelength. The XUV and NIR pulses were focused with a variable pulse delay onto the target, which comprised neon atoms and ethyl iodide molecules. Photoelectrons were generated by XUV ionization and propagated within the respective molecular or atomic potential, superimposed by the NIR laser field, which ponderomotively alters the electrons' momenta. The pulse-delay-dependent momentum distributions of photoelectrons were detected with a time-of-flight (TOF) spectrometer.

As an example for the experimental results from streaking measurements (also see Extended Data Fig. 1), Fig. 2a shows a streaking spectrogram obtained with 93 eV photons, in which two strong and one faint contributions can be discerned that oscillate with the pulse delay. The faint contribution near 80 eV arises (Fig. 2f) from valence emission from ethyl iodide. Analysis of the valence emission is not informative, because ionization can take place from a total of six orbitals within the bandwidth of the IAP¹⁸. Owing to the multi-orbital contributions, the photoelectron valence emission yields a broad spectral feature with no distinct spectral peak. In contrast, the trace at around 71.5 eV stems from photoionization from the neon 2p subshell. The large photoionization cross-section for neon atoms¹⁹ permits a clear identification of the neon 2p peak and

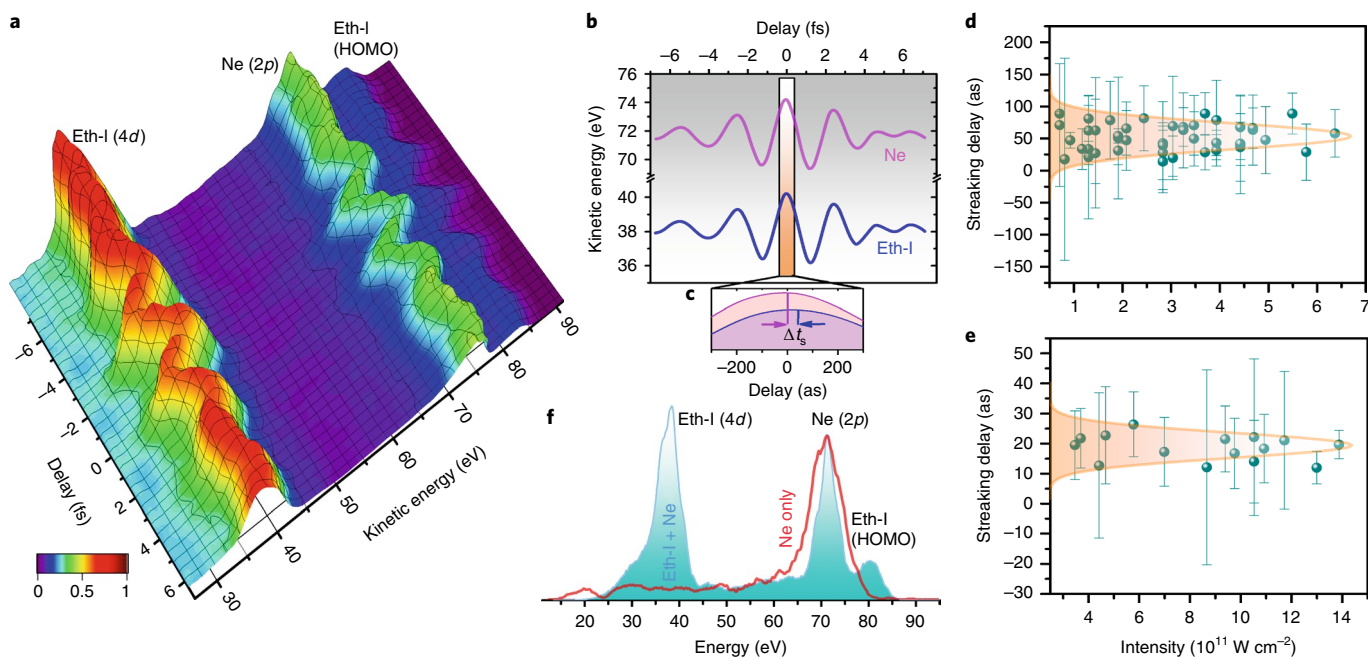


Fig. 2 | Ethyl iodide and neon streaking measurements. **a**, Attosecond streaking spectrograms measured for neon and ethyl iodide (Eth-I) for a photon energy centred at 93 eV. **b**, Streaking traces obtained from the spectrograms by ML analysis, followed by Fourier filtering. **c**, Enlarged view of the streaking time shift between the neon 2p and ethyl iodide 4d photoionization. **d,e**, Relative streaking delays between neon 2p and ethyl iodide 4d from different measurements at 80 and 93 eV, respectively, as a function of NIR intensity calculated from the amplitude of the corresponding streaking curves. Error bars indicate the variation in relative streaking phase delay in individual measurements. Gaussian fits (shaded areas) to the streaking delay distributions yield mean values and standard deviations of 51.8 ± 21.2 and 18.5 ± 4.3 as, respectively. **f**, Normalized XUV only (no NIR) photoelectron spectra for ethyl iodide with neon (shaded area) and for neon only (red curve) evidence the negligible contribution of neon 2s photoelectrons. HOMO, highest occupied molecular orbital.

a good signal-to-background ratio with respect to the partially overlapping ethyl iodide valence electrons. The contribution at around 37.5 eV in the photoelectron spectrum is attributed to the emission from the 4d subshell of iodine in ethyl iodide. A potential contribution from neon 2s in this energy region is negligible (Fig. 2f). The obtained binding potential at around 55.5 eV for the 4d emission band is in close agreement with literature values of 4d ionization from atomic iodine^{20,21}. In the experiments, the probed molecules experienced NIR laser intensities of around 10^{11} – 10^{12} W cm⁻², for which laser-induced distortions of the molecule's electronic structure can be safely neglected. Note that all the recorded NIR-induced above-threshold ionization contributions are below 16 eV, and do not overlap with the interrogated bands shown in Fig. 2a.

To extract streaking traces from the measured spectrograms for different bands, we utilized machine learning (ML). For the training of the ML approach (Methods gives details), the initial parameters were kept as randomized as possible: for example, up to ten streaking features were considered with random initial parameter-like positions, widths, intensities and streaking frequencies, within reasonable bounds, followed by the addition of a random jitter. The desired outputs of the algorithm were the streaking traces of each band in combination with their intensity and width. This trained ML algorithm was applied to the experimental streaking spectrogram to simultaneously extract streaking traces for all discernible bands. To complement this approach, another established model, namely non-negative least square (NNLS)²² optimization (Methods gives details) was also applied to extract streaking traces, which resulted in almost identical outputs with those of the ML approach. These approaches treat the image as a whole and identify streaking patterns not only at the current delay step of the scan, but also by a combination of multiple previous and upcoming electron spectra. This makes the algorithm less sensitive to noise and allows us

to extract streaking traces from low-intensity signals in a more reliable way.

To evaluate the relative streaking time delay of the ethyl iodide 4d emission, we calculated the phase delay relative to the neon 2p emission by transforming these retrieved streaking traces into the Fourier domain (details in the Methods and Extended Data Fig. 2). The Fourier-filtered data in the temporal domain, in which components outside the incident NIR frequency range are omitted, are shown in Fig. 2b for the neon 2p and ethyl iodide 4d emission. From the spectral phases of the neon and ethyl iodide streaking traces, we calculated the relative streaking phase delay according to:

$$\Delta t_s = \frac{\phi^{I4d}(\omega) - \phi^{Ne2p}(\omega)}{\omega} \quad (1)$$

where $\phi(\omega)$ represents the spectral phase of the ethyl iodide and neon streaking traces and ω describes the laser angular frequency. Using the spectral intensity of the neon streaking trace $I_{Ne}(\omega)$ as a weighting function, the relative streaking time delay Δt_s for each measurement is calculated by averaging over the streaking phase delay values:

$$\Delta t_s = \frac{\sum_{\omega} I_{Ne}(\omega) \Delta t_s(\omega)}{\sum_{\omega} I_{Ne}(\omega)} \quad (2)$$

The obtained results for different measurements at 80 and 93 eV are depicted in Fig. 2d,e, respectively, as a function of NIR intensity. It is evident that the delays are insensitive to the NIR intensity within the covered range, which designates insubstantial polarization effects and distortions of the molecule. This also shows that the results are robust against partial contamination with above-threshold ionization signals, especially at 80 eV. Average mean values and standard

deviations of the relative streaking delays were obtained from this data with 51.8 ± 21.2 as (80 eV) and 18.5 ± 4.3 as (93 eV). Given the different orders of magnitude between streaking delay and the period of the NIR field, the small streaking delay is only discernible on close inspection of the streaking traces, as illustrated in Fig. 2c.

To validate the above approaches, which we introduced here to extract streaking traces, we also retrieved the streaking curves by calculating the central energy after fitting Gaussian functions to the photoelectron spectrum at each delay step for individual bands. The resultant relative streaking delay value (Fig. 3) at 80 eV, after following the same Fourier analysis as described above, turns out to be nearly same, but with a much larger standard deviation (50.8 ± 35.8 as), whereas for 93 eV the value (17.4 ± 5.6 as) remains very similar to that of the ML approach. This clearly indicates the consistency and success of the ML analysis, especially for the noisier data at 80 eV. Both the analyses indicate the spectral broadening of the emission structure of ethyl iodide 4d, which can be attributed to the spin-orbit splitting of the 4d photoelectron band, with two components ($4d_{5/2}$ and $4d_{3/2}$) separated by 1.7 eV (ref. 23), which are not resolved because of the bandwidth of the attosecond pulse. However, we note that the relative photoionization delays between photoemission from the two spin-orbit components of iodine 4d are expected to be similarly small as those measured in the case of xenon 4d with -4.0 ± 4.1 as (ref. 24).

In Fig. 3a, we compare the experimental streaking delays to the theoretical predictions using the Classical Wigner Propagation (CWP) method^{11,25}, where the electronic structures of the ground states of ethyl iodide and neon are calculated either based on frozen-core Hartree-Fock (HF) or configuration interaction singles (CIS) formalisms. Here we have added an experimental data point at 105 eV, which was extracted from Ossiander et al.²⁶. In the first step of the CWP method, a bound electron is ionized into the continuum following the absorption of a single photon from the weak attosecond XUV pump pulse. This process is well-described within first-order perturbation theory. In the second step, the wavefunction of the photoionized electron is propagated in the presence of the NIR laser field by a classical Wigner propagator within the dipole approximation (for a detailed description of CWP formalism, see Methods, Vos et al.¹¹ and Zimmermann et al.²⁵). From the simulated spectrograms, the relative streaking phase delay and subsequently the relative streaking delay for ethyl iodide photoemission were calculated following the same analysis scheme described above for the experimental data. As this approach incorporates effects induced by Coulomb-laser coupling (CLC)²⁷⁻²⁹, illustrated in the inset to Fig. 3a, the simulated results are directly comparable to the experimental delay values. The calculations yield nearly overlapping values from HF and CIS, which indicates negligible contributions of excited states. Both HF and CIS simulations agree very well with the experimental measurements at higher energies and are well within the standard deviation for the lowest energy measurement at 80 eV.

In addition to the CWP calculations, we used an independent theoretical approach, based on molecular quantum scattering theory (QST), described in detail in Baykusheva and Wörner³⁰. According to this approach, the photoionization delay as a function of electron energy and emission direction in the molecular frame is defined as the energy derivative of the phase associated with the photoionization transition matrix element. The latter is calculated using the molecular orbitals of the neutral molecule obtained from HF calculations and the electronic continuum wavefunctions obtained through the variational Schwinger method. Hence, the QST approach directly provides the EWS delay, which can be compared to experiment after the CLC term is added to the latter. To describe the full dynamics in the laboratory frame, the calculated delays were isotropically averaged over all the molecular orientations. For a better comparison with the experimental findings, the results from the full QST were additionally averaged over

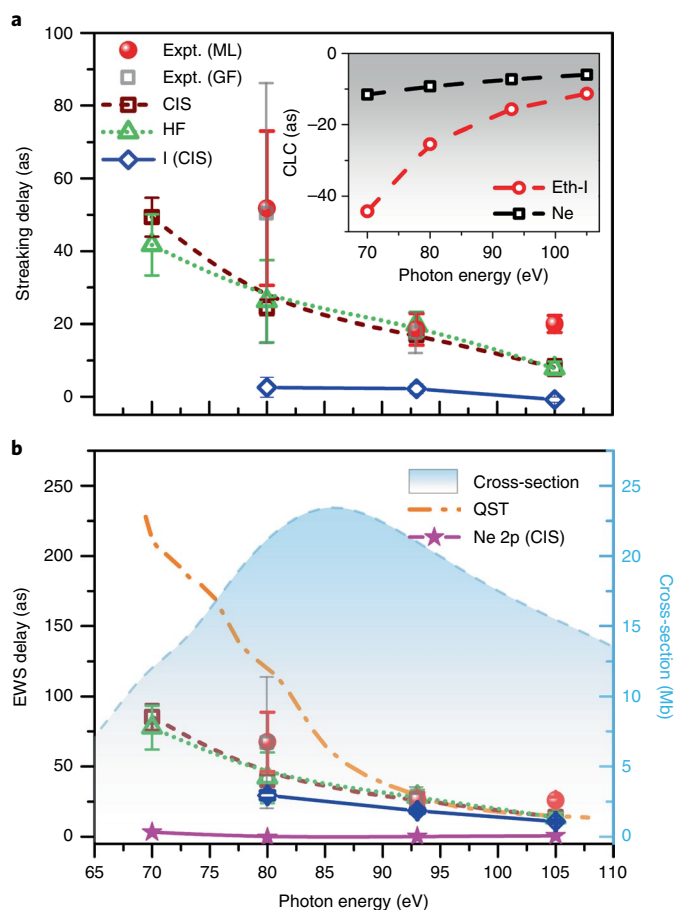


Fig. 3 | Streaking and EWS photoemission delays. a, Streaking delay for ethyl iodide 4d emission relative to neon 2p emission as a function of photon energy. The red dots represent the results from the ML analysis, whereas the grey squares represent results from analysis using Gaussian fitting (Extended Data Fig. 4). The brown square and green triangle symbols correspond to the CWP approach using CIS and HF formalisms, respectively. The blue diamond symbols represent the CIS results for atomic iodine. Inset: the CLC contributions for neon and ethyl iodide calculated according to Pazourek et al.¹⁴. The delay at 105 eV is extracted from Ossiander et al.²⁶. **b**, Comparison of EWS delay between different theoretical calculations and experimental data. The theory includes the QST calculation and Wigner approaches using HF and CIS for ethyl iodide. To determine the absolute EWS delays from the relative streaking delays for the experimental data and the CWP results, the neon 2p EWS delays calculated using the CIS model were added after the CLC correction. In the background, the photoionization cross-section (calculated using TD-LDA³¹) is shown, labelled on the right vertical axis. In both the panels error bars represent the corresponding standard deviations.

photoelectron emission directions, whereby the range was determined by the detector's acceptance angle in the experiment (a cone with a 45° full-opening angle around the NIR laser polarization).

The EWS delays predicted by QST and CWP calculations for ethyl iodide are compared to the experimental data in Fig. 3b. For experimental data and the CWP simulations, the CLC contribution, as shown in Fig. 3a inset, evaluated according to Pazourek et al.¹⁴, is subtracted from the relative streaking delay. The CLC contribution is due to the long-range Coulomb interaction between the departing electron and the positively charged parent ion, and is therefore nearly identical across all atoms and molecules, for a given electron energy. The EWS delays for neon 2p, calculated using the CIS formalism and added to the relative streaking values along with the

CLC subtraction to obtain the absolute EWS delay, are shown for comparison, and yield nearly negligible contributions over the studied energy range. In general, within the investigated energy region, both theoretical models predict positive EWS delays thus matching the conclusions of the calculations in refs. ^{30,31}, and a universal increase of EWS delays with decreasing photon energy, in accordance with the experimental findings.

We found that both theories make very similar predictions at higher energies and disagree somewhat at lower energies, with the experimental data point at 80 eV falling closer to the CWP predictions compared to the QST prediction for EWS delays. At higher energies, all the theoretical predictions match excellently with the experimental findings. The disagreement at lower energies can be understood by considering that accurate theoretical estimates become much more difficult at lower energies due to the increased influence of the short-range molecular potential on the wavefunction of the ionized electron, which is difficult to capture in all its complexity, particularly for polyatomic molecules. Although more difficult to measure experimentally and model theoretically, the lower energy data are very valuable as they contain a wealth of information, encoded in the EWS delay, about the short-range potential landscape. As can be seen from Fig. 3b, this short-range potential leads to a substantial additional delay of around 38.0 ± 21.4 as.

Generally, the rise in the EWS delay is expected for both shape and giant $4d$ resonances. For giant resonances, the intershell and intrashell interactions can influence the photoemission delay and this particular contribution was debated in prior theoretical works^{31,32}. In addition to the delay being due to the transient trapping of the electron wavefunction, such as observed in a shape resonance⁷, electron correlations can also play an important role³¹. For instance, short-range electron–electron repulsion can offset the negative CLC term (shown in the inset to Fig. 3a).

In contrast to the valence electron emission studied so far in most of the previous works^{7,11,15}, the giant dipole resonance in ethyl iodide is due to ionization from an inner $4d$ shell of the constituent iodine atom. As such, the ionized electron wavepacket is spatially localized near the iodine end of the molecule at the time of ionization and the ionization process is barely affected by the molecular environment. This is reflected well in the comparison between the phase space representations of the initial giant resonance ionization steps for atomic iodine and ethyl iodide, as shown in Fig. 4a–d. It can be seen that the first ionization step is very similar for the atom and the molecule. This implies that the escaping electron can probe the molecular landscape introduced by the remaining molecular fragment (that is, the ethyl group (Fig. 1a)) as it traverses through it. The comparison of the experimentally measured streaking delay and EWS delay for ethyl iodide with the theoretical values for ethyl iodide and atomic iodine, presented in Fig. 3a,b, expresses the molecular influence. We note that, experimentally, atomic iodine needs to be obtained from a molecular precursor, a process that is inefficient and causes overlap between the atomic and molecular signals. We thus rely here on theoretical data for atomic iodine using the previously tested CWP formalism^{11,25}. As the initial ionization step, and its contribution to the streaking or EWS delay, is virtually the same (resulting from ionization of the inner shell of iodine), the difference between ethyl iodide and atomic iodine is due to the subsequent propagation step of the electron within the molecular potential. This can be identified exclusively as the impact of the molecular potential on the departing electron wavepacket. Figure 3a,b clearly show an overall shift of the streaking delay as well as EWS delay in the case of ethyl iodide compared to that of iodine. At the lowest energy, the EWS delay shift is around 38.0 ± 21.4 as, which decreases with increasing photon energy. The theoretical estimates also show an overall shift, however, with a decreased magnitude at the lowest photon energy. The decrease in shift with increasing photon energy is expected because the higher-energy XUV generates

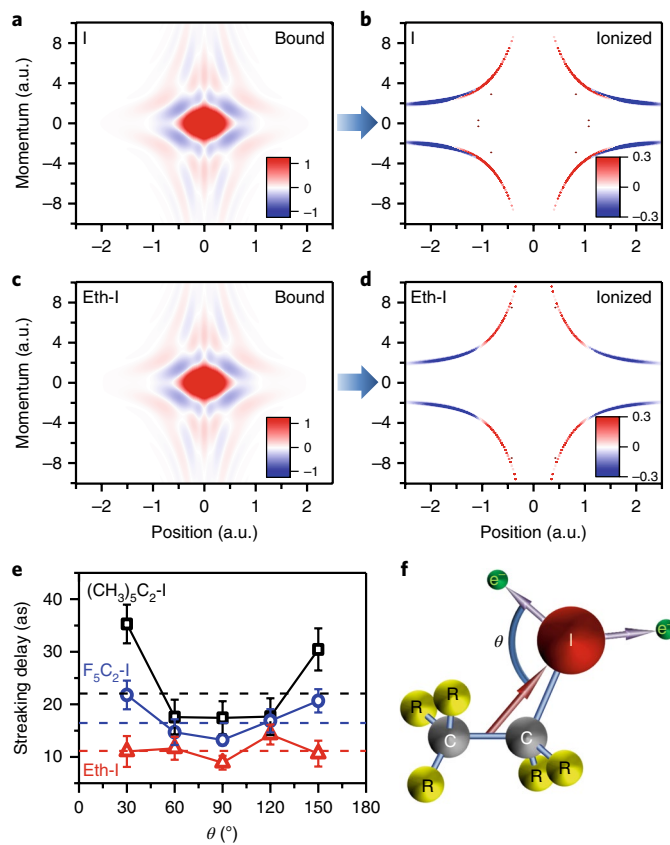


Fig. 4 | Comparison of the first step in the ionization process and molecular influence on photoemission delay. **a–d**, Wigner phase-space distribution, which shows a coordinate and momentum representation of an electron wavepacket, for the dipole transition from the ‘bound’ (**a,c**) to the ‘ionized’ (**b,d**) states of $4d \rightarrow 4f$ transitions of the electron during the giant dipole resonance inside the iodine atom (**a,b**) and ethyl iodide (**c,d**). The ionized state serves as a source function that provides the initial conditions for classical propagation (the second step). As can be seen from the figure, the quantum-mechanically calculated first step, which corresponds to transition from the bound to the ionized state, looks very similar for the atom and molecule in the case of a giant dipole resonance. The origin denotes the location of the iodine atom. Detailed information on the computation is provided in Methods. **e**, Angular distribution of the streaking delay (error bars represent the standard deviation) for different molecules obtained from Wigner calculations (CIS). **f**, In the molecules, the angle θ is measured with respect to the line between the C–C bond centre and iodine atom, shown by the red arrow, where R represents H, F or CH_3 . The angle-averaged streaking delay values are also shown as dashed horizontal lines in **e**.

photoelectrons of a higher kinetic energy, which spend less time in the molecular environment compared to the lower kinetic energy photoelectrons. As a result, the lower-energy electrons are influenced more by the molecular potential, which is manifested as a larger delay difference compared to the atomic iodine.

The influence of the molecular environment in other, related systems was studied theoretically, as shown in Fig. 4e. The data were calculated within the classical Wigner CIS formalism and show the effect of a variable ligand attached to the iodine atom. For ethyl iodide, the distribution is nearly isotropic. As the ligand mass increases, however, the angular-dependent photoemission delays are less flat. With an iodine atom as a reference, we expect an isotropic distribution, which is actually still seen for ethyl iodide, most probably because the statistical resolution of the calculation

is insufficient to capture a weak angular dependence. For the other two molecules, the delay is minimal for normal electron ejection whereas it increases as the photoionized electron escapes in the direction of the ligand or opposite to it. This difference can be attributed to the influence of the molecular environment. Here, we also show the angle-integrated delay values for these molecules (dashed horizontal lines in Fig. 4e), which manifest an increase of the overall delay with the size of the ligand and enable us to observe the molecular influence even without angular-resolved measurements.

Conclusions and outlook

We found that the ionization delay of an escaping electron wavepacket around a giant dipole resonance increases substantially due to the presence of a functional group. This is particularly important when one considers that, out of all the halogens, iodine has the lowest electronegativity. As a result, the attached alkyl group is close to neutral, which suggests that even a neutral ligand can measurably modify the potential landscape seen by the departing electron. Therefore, the photoemission delay provides sensitive information about the role of a functional group in a molecule, which cannot be obtained by the usual technique of measuring ionization cross-sections.

The correlation between the ionization delay and the size of the attached functional groups, as predicted by the angular-resolved simulations, opens up new perspectives for angle-resolved photoemission delay measurements in molecules to probe the potential landscape in three dimensions. Finally, as functional groups determine the characteristic chemical properties of a molecule, to understand their influence on ionization delays is crucial for the ultimate goal of steering chemical reactions using attosecond pulses³³.

Online content

Any methods, additional references, Nature Research reporting summaries, source data, extended data, supplementary information, acknowledgements, peer review information; details of author contributions and competing interests; and statements of data and code availability are available at <https://doi.org/10.1038/s41567-020-0887-8>.

Received: 21 December 2018; Accepted: 20 March 2020;
Published online: 11 May 2020

References

- Krausz, F. & Ivanov, M. Attosecond physics. *Rev. Mod. Phys.* **81**, 163–234 (2009).
- Wigner, E. P. Lower limit for the energy derivative of the scattering phase shift. *Phys. Rev.* **98**, 145–147 (1955).
- Cavalleri, A. L. et al. Attosecond spectroscopy in condensed matter. *Nature* **449**, 1029–1032 (2007).
- Ossiander, M. et al. Attosecond correlation dynamics. *Nat. Phys.* **13**, 280–285 (2016).
- Schultze, M. et al. Delay in photoemission. *Science* **328**, 1658–1662 (2010).
- Seiffert, L. et al. Attosecond chronoscopy of electron scattering in dielectric nanoparticles. *Nat. Phys.* **13**, 766–770 (2017).
- Huppert, M., Jordan, I., Baykusheva, D., von Conta, A. & Wörner, H. J. Attosecond delays in molecular photoionization. *Phys. Rev. Lett.* **117**, 093001 (2016).
- Isinger, M. et al. Photoionization in the time and frequency domain. *Science* **358**, 893–896 (2017).
- Klüber, K. et al. Probing single-photon ionization on the attosecond time scale. *Phys. Rev. Lett.* **106**, 143002 (2011).
- Tao, Z. et al. Direct time-domain observation of attosecond final-state lifetimes in photoemission from solids. *Science* **353**, 62–67 (2016).
- Vos, J. et al. Orientation-dependent stereo Wigner time delay and electron localization in a small molecule. *Science* **360**, 1326–1330 (2018).
- Haessler, S. et al. Phase-resolved attosecond near-threshold photoionization of molecular nitrogen. *Phys. Rev. A* **80**, 011404(R) (2009).
- Dahlström, J. M., L'Huillier, A. & Maquet, A. Introduction to attosecond delays in photoionization. *J. Phys. B* **45**, 183001 (2012).
- Pazourek, R., Nagele, S. & Burgdörfer, J. Attosecond chronoscopy of photoemission. *Rev. Mod. Phys.* **87**, 765–802 (2015).
- Kamalov, A., Wang, A. L., Bucksbaum, P. H., Haxton, D. J. & Cryan, J. P. Electron correlation effects in attosecond photoionization of CO₂. Preprint at <http://arXiv.org/1906.10728> (2019).
- Connerade, J. P. et al. in *Giant Resonances in Atoms Molecules and Solids* (eds Connerade, J. P., Esteve, J. M. & Karnatak, R. C.) 3–23 (Nato Science Series Vol. 151, Springer, 1987).
- Amusia, M. Y., Cherepkov, N. A., Chernysheva, L. V. & Manson, S. T. Photoionization of atomic iodine and its ions. *Phys. Rev. A* **61**, 020701(R) (2000).
- Katsumi, K., Shunji, K., Yohji, A., Hiroshi, M. & Saburo, N. Photoelectron spectra and orbital structures of higher alkyl chlorides, bromides, and iodides. *Bull. Chem. Soc. Jpn* **46**, 373–380 (1973).
- Sewell, K. G. Photoionization cross section of neon. *Phys. Rev.* **138**, A418–A421 (1965).
- Eland, J. H. D. et al. Dissociation of multiply charged ICN by Coulomb explosion. *J. Chem. Phys.* **145**, 074303 (2016).
- Schnorr, K. *XUV Pump-Probe Experiments on Diatomic Molecules: Tracing the Dynamics of Electron Rearrangement and Interatomic Coulombic Decay* (Springer International, 2015).
- Lawson, C. L. & Hanson, R. J. *Solving Least Squares Problems* (Society for Industrial and Applied Mathematics, 1995).
- Nahon, L., Svensson, A. & Morin, P. Experimental study of the 4d ionization continuum in atomic iodine by photoelectron and photoion spectroscopy. *Phys. Rev. A* **43**, 2328–2337 (1991).
- Jain, A., Gaumnitz, T., Bray, A., Kheifets, A. & Wörner, H. J. Photoionization delays in xenon using single-shot referencing in the collinear back-focusing geometry. *Opt. Exp.* **43**, 4510–4513 (2018).
- Zimmermann, T., Ortmann, L., Hofmann, C., Rost, J. M. & Landsman, A. S. Attosecond streaking delays in multi-electron systems. Preprint at <http://arXiv.org/1804.09583> (2018).
- Ossiander, M. et al. Absolute timing of the photoelectric effect. *Nature* **561**, 374–377 (2018).
- Nagele, S. et al. Time-resolved photoemission by attosecond streaking: extraction of time information. *J. Phys. B* **44**, 081001 (2011).
- Pazourek, R., Feist, J., Nagele, S. & Burgdörfer, J. Attosecond streaking of correlated two-electron transitions in helium. *Phys. Rev. Lett.* **108**, 163001 (2012).
- Pazourek, R., Nagele, S. & Burgdörfer, J. Time-resolved photoemission on the attosecond scale: opportunities and challenges. *Faraday Disc.* **163**, 353–376 (2013).
- Baykusheva, D. & Wörner, H. J. Theory of attosecond delays in molecular photoionization. *J. Chem. Phys.* **146**, 124306 (2017).
- Pi, L.-W. & Landsman, A. Attosecond time delay in photoionization of noble-gas and halogen atoms. *Appl. Sci.* **8**, 322 (2018).
- Maia, M. & Himadri, C. Attosecond time delays in the valence photoionization of xenon and iodine at energies degenerate with core emissions. *J. Phys. Conf. Ser.* **875**, 022015 (2017).
- Corkum, P. B. & Krausz, F. Attosecond science. *Nat. Phys.* **3**, 381–387 (2007).
- Comes, F. J., Nielsen, U. & Schwarz, W. H. E. Inner electron excitation of iodine in the gaseous and solid phase. *J. Chem. Phys.* **58**, 2230–2237 (1973).
- Lindle, D. W. et al. Inner-shell photoemission from the iodine atom in CH₃I. *Phys. Rev. A* **30**, 239–244 (1984).

Publisher's note Springer Nature remains neutral with regard to jurisdictional claims in published maps and institutional affiliations.

© The Author(s), under exclusive licence to Springer Nature Limited 2020

Methods

Experimental set-up. The laser set-up and attosecond beamline at the Attosecond Science Laboratory of the King Saud University are described elsewhere³⁶. Briefly, the pulses used in the experiment were delivered by a commercial laser system (FEMTOPOWER compact PRO HP/HR 3kHz, Spectra Physics). The system delivers carrier-envelope phase-stable 25 fs pulses with an energy of up to 800 μ J. The pulses were spectrally broadened in a hollow-core fibre filled with neon to a width of 300 nm centred at 750 nm, supporting sub-two-cycle pulses. The pulses were subsequently compressed by a set of chirped mirrors. Finally, phase-stable few-cycle pulses of duration around 4.7 fs with 350 μ J at a 3 kHz repetition rate were delivered to the experiment. In the attosecond beamline, XUV light was generated via high-harmonic generation, whereafter XUV and fundamental NIR beams were spatially separated with a concentric Zr-foil filter and a double mirror that focused both beams onto the target. The coating of the inner mirror, which focuses the XUV beam, supported a bandwidth of 6.5 eV around different central photon energies selected in the cutoff region of the high-harmonic generation spectrum. The XUV–NIR pulse delay could be adjusted with a piezo stage attached to the inner mirror. The target gases were delivered to the interaction volume through a thin nozzle. The gas mixture was prepared within an external bubbler system, where the neon gas went into the ethyl iodide liquid through an input tube, and the neon–ethyl iodide mixture evaporated and was guided to the gas nozzle by an output tube. The ionized electrons were captured by a TOF spectrometer equipped with an electrostatic lens and microchannel plate detector at the end.

Retrieval of streaking delay. To extract the streaking traces from the experimental streaking spectrogram, a total of three approaches were adapted. First, out of a measured streaking spectrogram, the streaking curves for different bands (ethyl iodide (*4d*), neon (*2p*) and ethyl iodide (HOMO)) were extracted using ML-based analysis. This involves extensive training of the algorithm with test datasets. The test datasets were created with parameters as general as possible and involved multiple streaking features (up to ten) at random positions, with random widths, intensities and streaking frequencies. At each delay slice, a random jitter was added to all the previous parameters. The trained algorithm, which produced the output as the traces that correspond to each band in combination with their intensity and width, was applied to the experimental data. Different models were applied on this training data with almost identical results for the analysis of the experimental data. One of the models is to learn the transformation $X \rightarrow Y$ via a multilayer neural network³⁷ with a drop rate to prevent overfitting³⁸. The second, more established, approach uses the assumptions put into the training data as conditions in an optimization routine. This analysis takes way more calculation time but does not use the training data at all. It was realized by NNLS optimization with a rather huge basis set of traces. In this NNLS optimization²², the (*L2*) regularization was achieved by a Tikhonov matrix shaped as identity scaled by a factor $\ll 1$. The NNLS algorithm is very similar to that used in Hartmann et al.³⁹. In essence, all these models and the applied training datasets proved robust against the reconstruction of all the streaking traces at once from an experimental streaking spectrogram.

In addition to the above analyses, as a third approach, we employed a manual analysis based on Gaussian curve fitting over the electron spectrum to identify the streaking traces. Corresponding to ethyl iodide *4d* and neon *2p* emissions, at each delay step Gaussian functions were independently fitted to the photoemission yields within a limited energy range around the respective peak maxima. The central energies that provided the best fits defined the streaking traces for the respective emission orbitals. For the neon streaking spectrogram, although it is marginally contaminated by the ethyl iodide valence electron emission, the large photoionization cross-section facilitates the ability to resolve the peak structure at any delay position. For the 80 eV data (Extended Data Fig. 3), a similar situation occurs for the ethyl iodide *4d* emission peak, which is marginally contaminated by above-threshold ionization electrons induced by the few-cycle laser field (Extended Data Fig. 5). However, using a reduced NIR intensity, and because of the large cross-section at the iodine giant resonance, the peak structure remains clearly distinguishable throughout the full delay range.

To retrieve the streaking time delays, streaking traces were Fourier transformed, after zero padding, into the spectral domain, which yielded the spectral amplitude and phase (Extended Data Fig. 2). As the phase and time shift are inherently connected, the relative streaking phase delay $\Delta t_s(\omega)$ between the two emission lines is calculated according to:

$$\Delta t_s(\omega) = \frac{\phi^{14d}(\omega) - \phi^{\text{Ne } 2p}(\omega)}{\omega} \quad (3)$$

where $\phi^{14d}(\omega)$ and $\phi^{\text{Ne } 2p}(\omega)$ represent the spectral phases of the ethyl iodide and neon streaking traces, respectively, and ω stands for the NIR laser angular frequency. The resulting relative streaking phase delay $\Delta t_s(\omega)$ is nearly a flat function of angular frequency (Extended Data Fig. 2), for which the average or the relative streaking delay is calculated according to:

$$\Delta t_s = \frac{\sum_{\omega} I_{\text{Ne}}(\omega) \Delta t_s(\omega)}{\sum_{\omega} I_{\text{Ne}}(\omega)} \quad (4)$$

where the spectral intensity ($I_{\text{Ne}}(\omega)$) for neon is used for averaging. The method of calculating delay from the scattering phase is well established, and has previously been used in, for example, Huppert et al.⁷ and Vos et al.¹¹ (Dahlström et al.¹³ and Pazourek et al.¹⁴ give details).

CWP method calculations. The photoelectron in the CWP method is described by the Wigner function, which is sampled by individual trajectories that are then propagated classically. The Wigner function itself is derived from the first-order perturbation theory wavefunction that describes the single-photon ionization of the electron by the XUV field. This approximation is justified by the relatively weak XUV pulses used in the streaking experiments. The single-electron zeroth-order wavefunction is determined from the Dyson orbital that corresponds to a chosen final ionic state. The interaction with the probe NIR field is then described non-perturbatively during the classical propagation. The detailed derivation of the method is presented in Zimmermann et al.²⁵ and further information can be found in the supplementary information of Vos et al.¹¹. Here we provide the specific parameters that were used to simulate streaking delays of the *4d* orbital in ethyl iodide.

The peak intensity of the XUV pulse used in the calculations did not play a role, and was arbitrarily set to 1 a.u. = 3.51×10^{16} W cm⁻². The envelope was Gaussian shaped with a full-width at half-maximum of around 260 as. The NIR pulse had a wavelength of 750 nm, an intensity of 8×10^{12} W cm⁻² and a Gaussian-shaped envelope with a full-width at half-maximum of 7 fs. Even though the intensities of the pump and probe pulses used in the simulations do not exactly match the experimental values, streaking delays are insensitive to the XUV and NIR intensities⁵ as long as multi-photon XUV ionization and NIR-induced initial state distortion can be neglected. Therefore, the results of the CWP simulations should be directly comparable with the experimental values.

The Dyson orbitals, given by the overlap of multielectron wavefunctions of the neutral molecule and of an ion with a missing *4d* electron, were computed using Superdyson⁴⁰. The neutral and ionized molecular wavefunctions were computed using the HF or CIS method (the latter allows for ionization only from *4d* orbitals) using a double-zeta 6-31G** or correlation-consistent triple-zeta basis set, respectively. For the CIS, the ORMAS program from the quantum-chemistry package Gamess was used⁴¹. The core electrons of iodine were described with a model core potential^{42,43}. The electrostatic forces between the ionized electron and the ion were computed from the one-particle density matrix derived from the HF or CIS wavefunction of the ion in the double-zeta 6-31G** basis or correlation-consistent double-zeta basis set, respectively. The polarization of the neutral molecule with the infrared field was neglected.

To simulate the streaking trace, 64 equally spaced pump–probe time delays were simulated with a time step of 400 as. Twelve orientations of ethyl iodide were used to mimic the random orientation of the molecule in the gas-phase experiment. The orientations sample the surface of the sphere evenly.

At each XUV-pulse central frequency, the final result of the simulation is a streaking trace. To simulate the detector used in the experiment, only trajectories in a detection cone of a 23° half-opening angle around the polarization axis were taken into account. To analyse the streaking traces and calculate the streaking delay, the same procedure that was used in the experimental data analysis was adapted. To estimate the standard deviation, we split all the trajectories that ended up in the detection cone randomly into ten different ensembles, calculated the delays with the above-described procedure separately for each ensemble and then computed the statistical spread of the results. The analysis was done separately for the two detection cones in opposite directions along the polarization axis and the final streaking delays were obtained by averaging the two results.

Calculation of the CLC term. The CLC corrections were calculated using the analytical formula given in equation (4.18) in Pazourek et al.¹⁴. Here the ionization potentials considered for ethyl iodide, atomic iodine and neon were 55.5, 57.1 and 21.6 eV, respectively.

QST calculations. Formally, the photoemission-direction and molecular-orientation-resolved one-photon (*1hν*) photoionization delay $\tau_{1h\nu}(E, \mathbf{k}, \mathbf{R})$ is defined as the energy (*E*) derivative of the phase of the photoionization matrix element $I_{i,f}$ connecting initial (*i*) and final (*f*) states (atomic units are employed):

$$\tau_{1h\nu}(E, \mathbf{k}, \mathbf{R}) = \frac{\partial}{\partial E} \arg(I_{i,f}) \quad (5)$$

where \mathbf{k} denotes the photoemission direction in the molecular frame and \mathbf{R} is a collective variable for the Euler angles that are used to transform the coordinate system from the molecular frame to the laboratory frame. The definition of the length-gauge photoionization matrix element $I_{i,f}$ is provided in equation (9.3) of Schultz and Vrakking⁴⁴. This quantity is calculated within a single-centre-expansion approach employing partial waves that are the energy-normalized solutions of the Lippmann–Schwinger equation defined in Lucchese and McKoy⁴⁵. The scattering calculations were performed using the program code ePolyScat^{46,47}. The HF wavefunction approximating the initial state of ethyl iodide was calculated employing an all-electron 6-311 G**–Pople basis set for all the atoms on the basis of an equilibrium geometry determined with the

second-order Møller–Plesset perturbation theory. The partial-wave expansion was truncated at a maximum partial-wave number of $l_{\max} = 50$.

The expression for $\tau_{1hv}(E, \mathbf{k}, \mathbf{R})$ in terms of the photoionization partial-wave matrix elements $I_{lm\mu}$ reads:

$$\tau_{1hv}(E, \mathbf{k}, \mathbf{R}) = \frac{\partial}{\partial E} \arg \sum_{lm\mu} I_{lm\mu} Y_{lm}(\mathbf{k}) D_{lm\mu}^1(\mathbf{R}) \quad (6)$$

where $Y_{lm}(\mathbf{k})$ is a spherical-harmonic function and $D_{lm\mu}^1$ denotes a Wigner D-matrix. In the above equation, the indices l and m denote the partial wave number and the corresponding magnetic quantum number, whereas $\mu (= 0, \pm 1)$ corresponds to a spherical tensor component. The subscript m_p specifies the laser polarization direction in the laboratory frame. For the case of linear polarization considered here, $m_p = 0$. To obtain the photoionization delay averaged over photoemission angles and molecular orientations, the angle-resolved delays were weighted by a factor proportional to the partial photoionization cross-section in the particular direction and summed³⁰:

$$\tau_{1hv} = \frac{1}{8\pi^2} \int d\mathbf{R} \int d\mathbf{k} \frac{\left| \sum_{lm\mu} I_{lm\mu} Y_{lm}(\mathbf{k}) D_{lm\mu}^1(\mathbf{R}) \right|^2}{\sum_{lm\mu} |I_{lm\mu}|^2} \frac{\partial}{\partial E} \arg \sum_{lm\mu} I_{lm\mu} Y_{lm}(\mathbf{k}) D_{lm\mu}^1(\mathbf{R}) \quad (7)$$

The integration over the two photoemission polar angles $\mathbf{k} = (\theta, \phi)$ and the Euler angles was performed by discretizing the integrand on two Lebedev quadrature grids of order 15 (86 points).

Data availability

The data represented in Figs. 1c, 2d,e, 3 and 4e are available as Source Data. All other data that support the findings of this study are available from the corresponding authors upon reasonable request.

Code availability

The codes that support the findings of this study are available from the corresponding authors upon reasonable request.

References

36. Schötz, J. et al. Phase-matching mechanism for high-harmonic generation in the overdriven regime driven by few-cycle laser pulses. Preprint at <https://arxiv.org/abs/1912.07918> (2019).
37. Rojas, R. *Neural Networks: A Systematic Introduction* (Springer, 1996).
38. Srivastava, N., Hinton, G., Krizhevsky, A., Sutskever, I. & Salakhutdinov, R. Dropout: a simple way to prevent neural networks from overfitting. *J. Mach. Learn. Res.* **15**, 1929–1958 (2014).
39. Hartmann, N. et al. Attosecond time–energy structure of X-ray free-electron laser pulses. *Nat. Photon.* **12**, 215–220 (2018).
40. Patchkovskii, S., Zhao, Z., Brabec, T. & Villeneuve, D. M. High harmonic generation and molecular orbital tomography in multielectron systems: beyond the single active electron approximation. *Phys. Rev. Lett.* **97**, 123003 (2006).
41. Schmidt, M. W. et al. General atomic and molecular electronic structure system. *J. Comp. Chem.* **14**, 1347–1363 (1993).
42. Miyoshi, E., Sakai, Y., Tanaka, K. & Masamura, M. Relativistic dsp-model core potentials for main group elements in the fourth, fifth and sixth row and their applications. *J. Mol. Struct. THEOCHEM* **451**, 73–79 (1998).
43. Sekiya, M., Noro, T., Osanai, Y. & Koga, T. Contracted polarization functions for the atoms Ca, Ga–Kr, Sr, and In–Xe. *Theor. Chem. Acc.* **106**, 297–300 (2001).
44. Schultz, T. & Vrakking, M. *Attosecond and XUV Physics: Ultrafast Dynamics and Spectroscopy* (Wiley-VCH, 2014).
45. Lucchese, R. R. & McKoy, V. Studies of differential and total photoionization cross sections of carbon dioxide. *Phys. Rev. A* **26**, 1406–1418 (1982).
46. Natalense, A. P. P. & Lucchese, R. R. Cross section and asymmetry parameter calculation for sulfur 1s photoionization of SF₆. *J. Chem. Phys.* **111**, 5344–5348 (1999).
47. Gianturco, F. A., Lucchese, R. R. & Sanna, N. Calculation of low-energy elastic cross sections for electron-CF₄ scattering. *J. Chem. Phys.* **100**, 6464–6471 (1994).

Acknowledgements

We acknowledge fruitful discussions with and support from F. Krausz. We are grateful for support from the King Saud University in the framework of the MPQ-KSU-LMU collaboration, and from the Researchers Supporting Project number RSP-2019/152. S.B. acknowledges support from the MULTIPLY fellowship program under the Marie Skłodowska-Curie COFUND Action and the Alexander von Humboldt Foundation. B.F. and J.S. acknowledge support from the Max Planck Society via the IMPRS-APS. M.F.K. is grateful for support from the Max Planck Society and the German Research Foundation via KL-1439/11-1.

Author contributions

S.B., B.F. and L.O. contributed equally to this work. S.B., B.F., J.S., W.S., H.A.M., I.L., A.M.K., N.G.K., A.F.A., M.A., A.M.A. and M.F.K. conducted the experiments. S.B. and B.F. did the data analysis. G.H. worked on the ML code and extracted streaking traces. L.O., T.Z. and A.S.L. did the CWP calculations. L.P. performed the TDLDA simulations. D.B. and H.J.W. did the QST calculations. S.B., B.F., L.O., T.Z., D.B., H.J.W., A.S.L. and M.F.K. wrote the manuscript, which was reviewed by all the authors.

Competing interests

The authors declare no competing interests.

Additional information

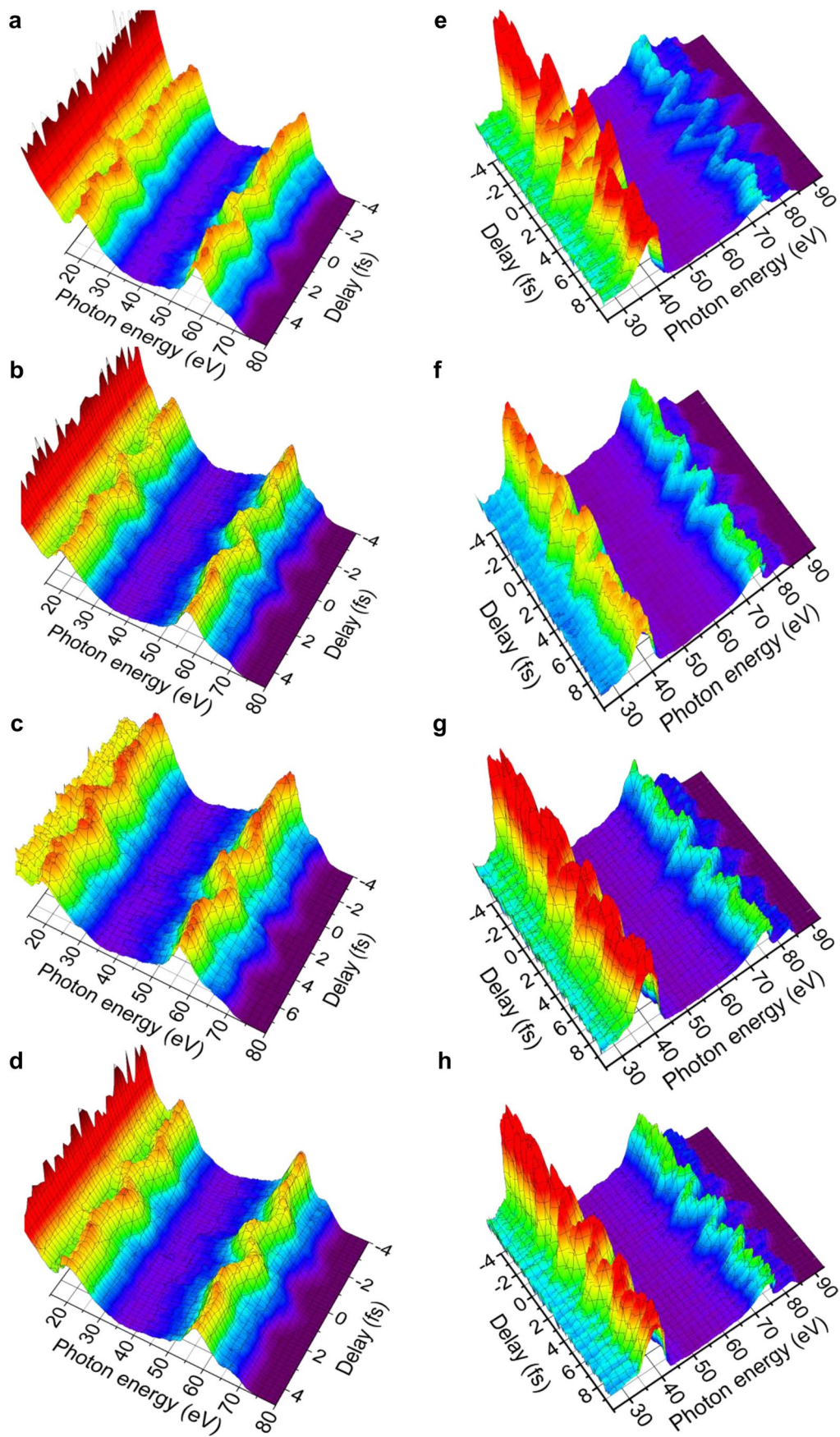
Extended data is available for this paper at <https://doi.org/10.1038/s41567-020-0887-8>.

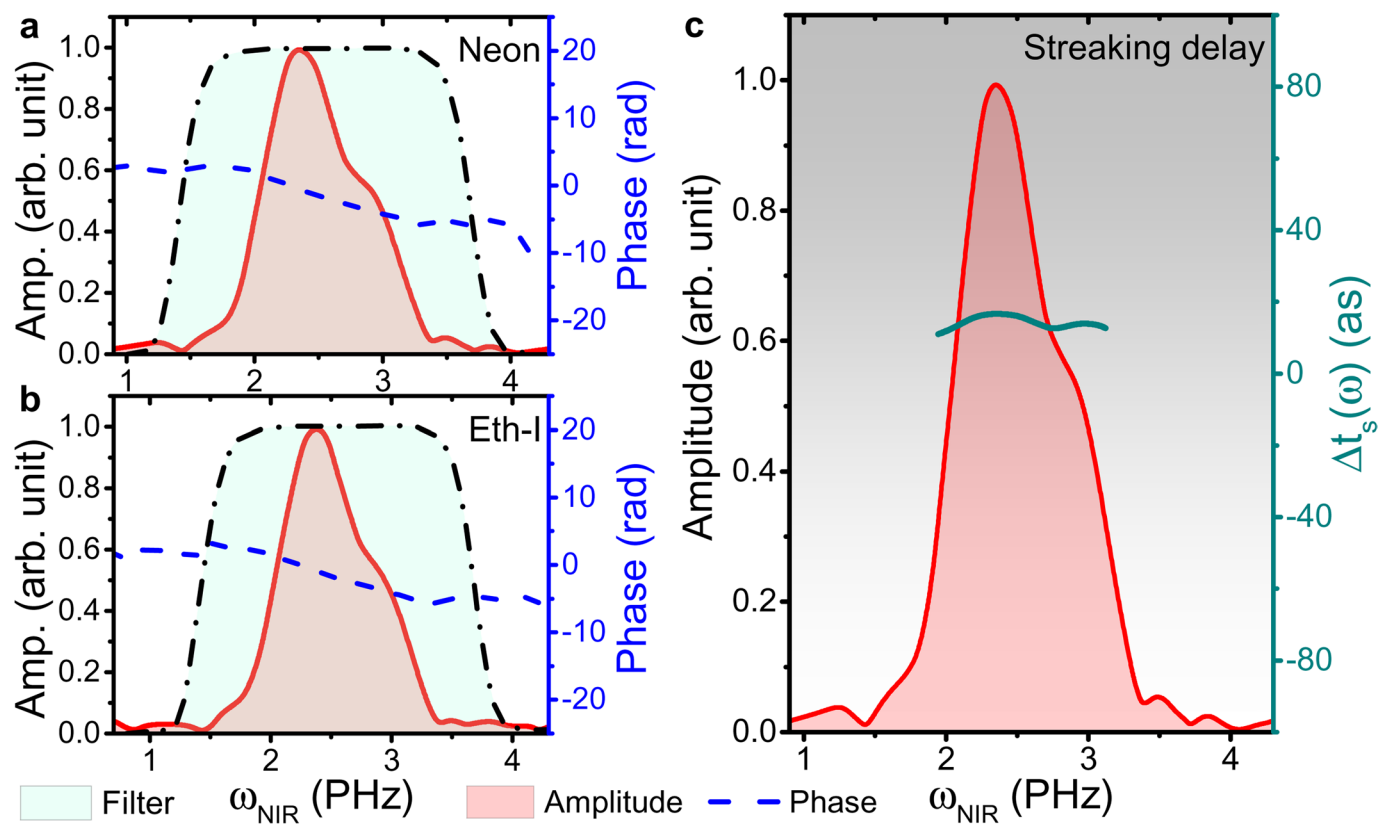
Supplementary information is available for this paper at <https://doi.org/10.1038/s41567-020-0887-8>.

Correspondence and requests for materials should be addressed to A.S.L. or M.F.K.

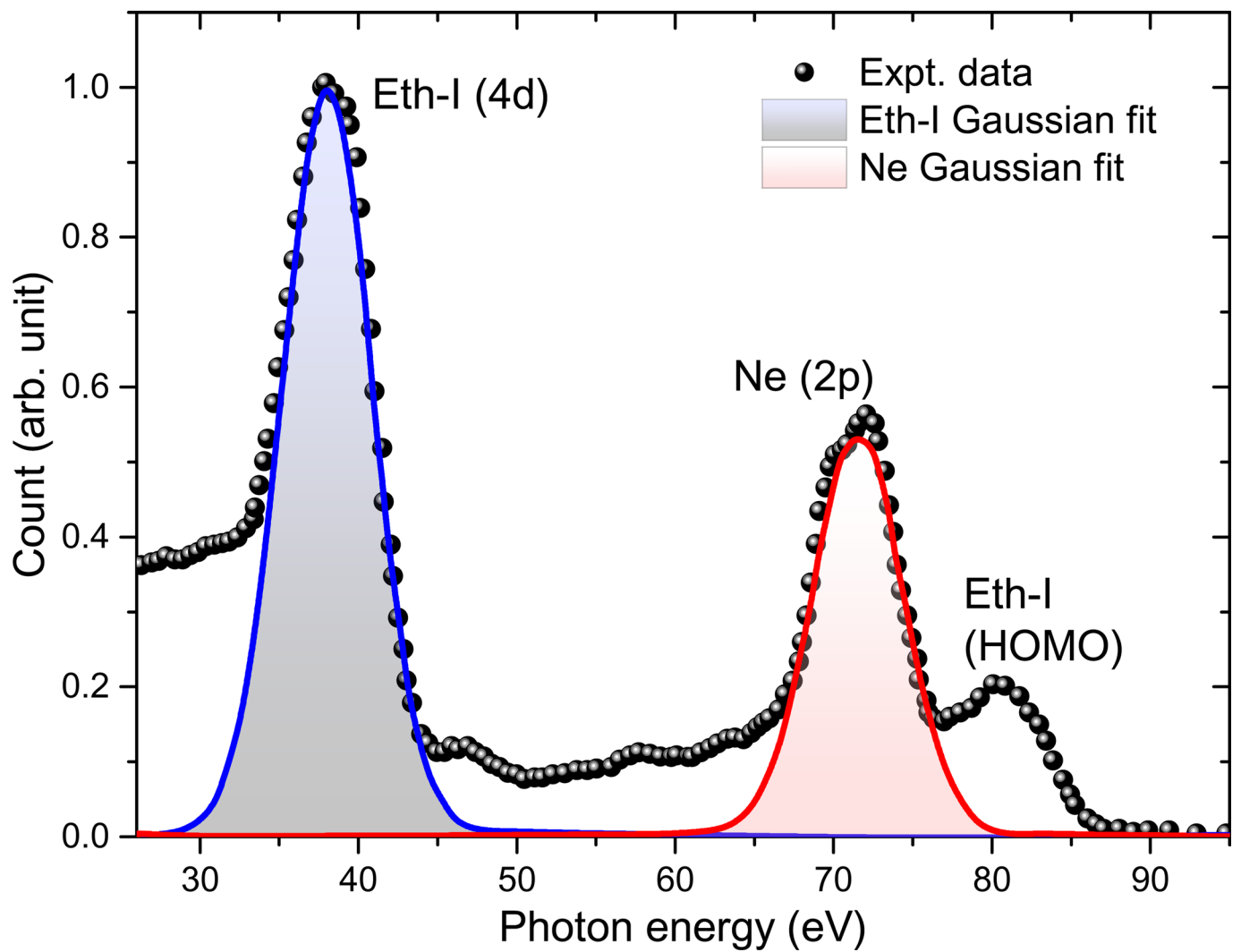
Peer review information *Nature Physics* thanks Renate Pazourek and the other, anonymous, reviewer(s) for their contribution to the peer review of this work.

Reprints and permissions information is available at www.nature.com/reprints.

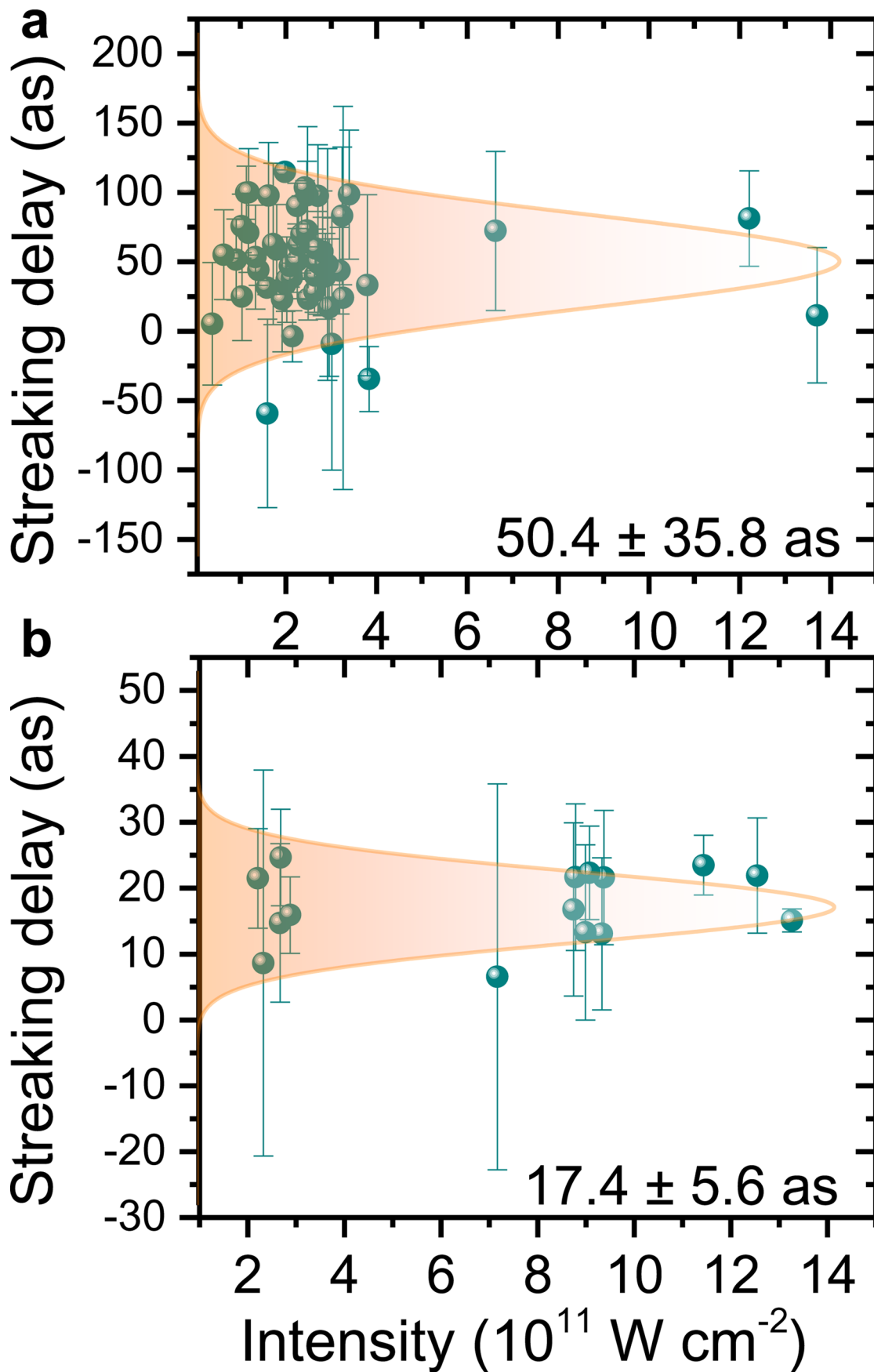




Extended Data Fig. 2 | Retrieval procedure of streaking delays. In (a) and (b) the spectral amplitude and phase of the streaking traces, retrieved from the neon 2p and iodine 4d emission, respectively, for the case of 93 eV XUV central energy, are displayed in dependence of the angular frequency ω of the NIR laser field. Spectral intensities below the threshold of $0.1I_{\text{max}}(\omega)$ (that is spectral amplitude threshold of $A(\omega) \leq \sqrt{0.1}A_{\text{max}}(\omega)$) are considered as noise level, for which the spectral phase $\phi(\omega)$ is blanked. The Fourier filter, which confines the respected angular frequency range to the NIR laser spectrum, is displayed as black dash-dotted line. In (c) the streaking phase delay $\Delta t_s(\omega)$, green solid line, calculated using Eq. 1 as described in the main text, is shown together with the filtered spectral amplitude of the neon streaking trace. The latter is used as weighting factor to calculate the weighted mean value Δt_s . Here, the streaking phase delay is determined for the frequency region for which the amplitude is above the threshold.

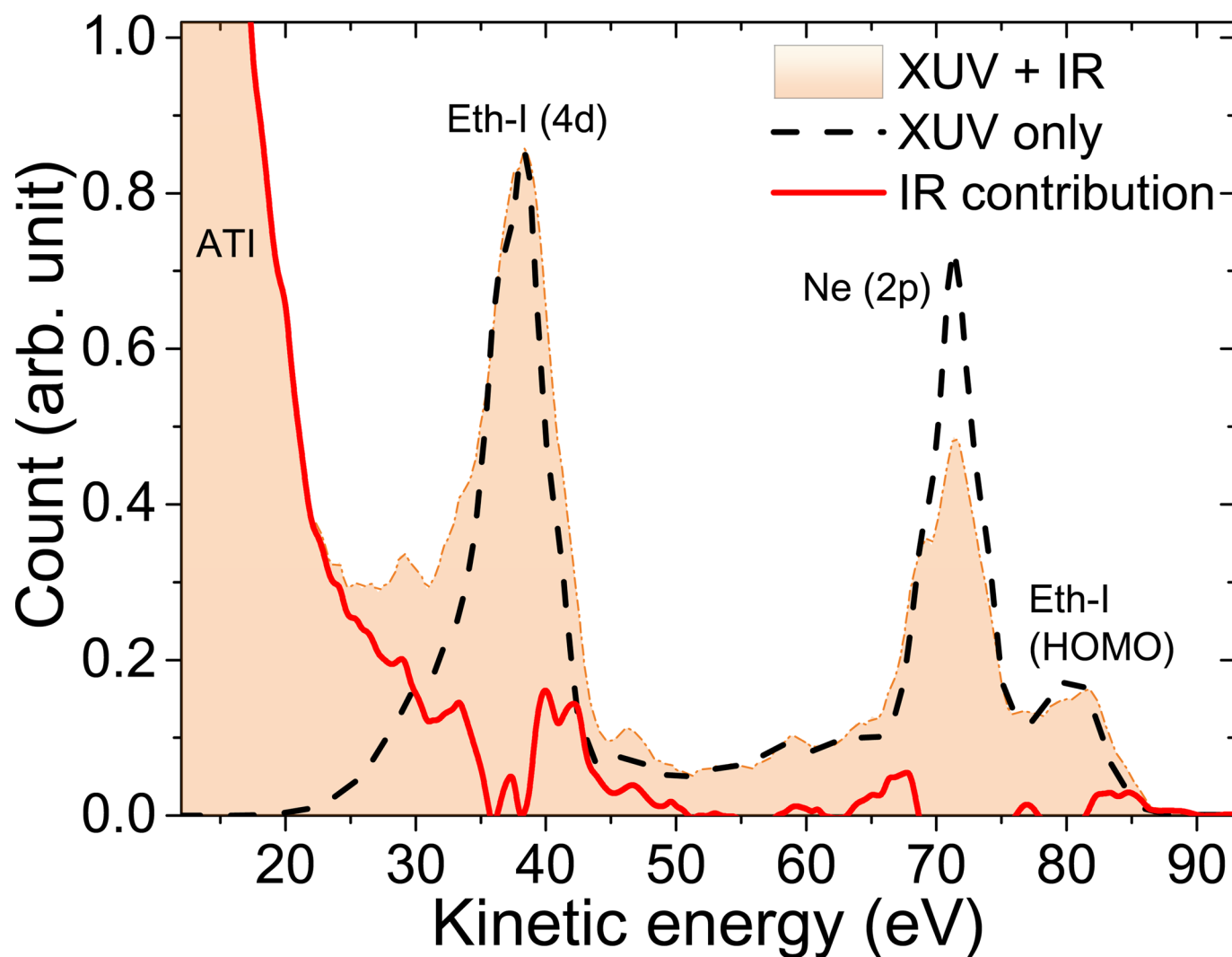


Extended Data Fig. 3 | Quality of Gaussian fitting in GF analysis. Independent Gaussian fitting for Ne and ethyl iodide peaks, used in GF analysis at 80 eV XUV photon energy.



Extended Data Fig. 4 | see next page for caption.

Extended Data Fig. 4 | Relative streaking delays derived from Gaussian fitting analysis. (a) and (b) Relative streaking delays, retrieved from Gaussian fitting analysis for results from measurements at 80 eV and 93 eV, respectively, as a function of NIR intensity calculated from the amplitude of the corresponding streaking curves. Error bars indicate the variation in relative streaking phase delay in individual measurements. This figure is complementary to Figs. 2(d) and (e) in the main text, which represent the results from machine learning analysis.



Extended Data Fig. 5 | Photoelectron spectra for XUV and NIR irradiation, and only XUV irradiation. The shaded data represents the spectrum for XUV and NIR irradiation together. The black dashed line represents the spectrum for XUV irradiation only. By subtracting this from the combined XUV+NIR data set, the NIR contribution (red line) can be estimated, and is found to mainly originate from ATI electrons at low energies.